Supplementary information of: Photoluminescence research of the graphene quantum dots (GQD) interaction on the zinc oxide (ZnO) surface for application as H_2O_2 photosensor

Rolando Efraín Ramírez Garza, Sara Luisa Rodríguez de Luna, and Idalia Gómez de la Fuente*

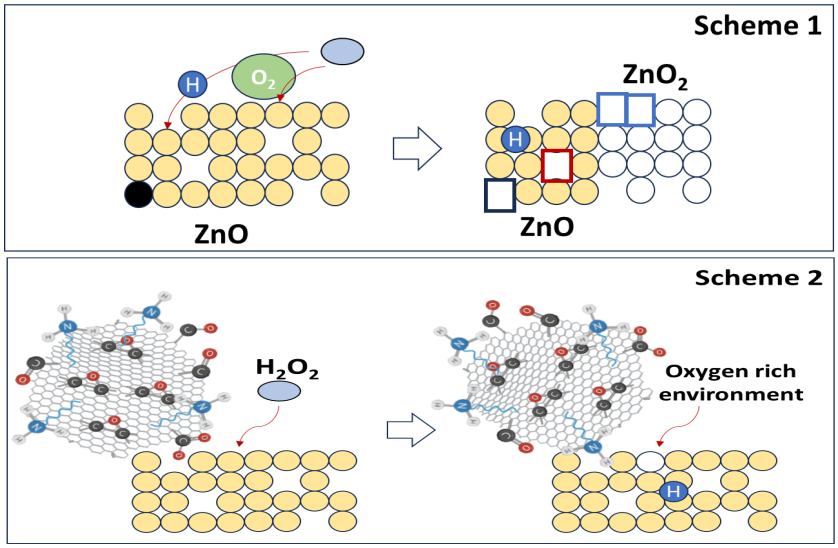

Fig. S1 Scheme 1: representation of the interaction between H_2O_2 and the solid ZnO; red square: native vacancies, black square: vacancies produced by calcination, blue square: vacancies due to oxidation of ZnO; "H": interstitial hydrogen, and white circles: represent the oxidation of ZnO to produce ZnO_2, Scheme 2: GQD interaction with ZnO to produce nanocomposites; oxygen from carboxyls in GQD interacts first with ZnO surface, until oxygen from H_2O_2 arrives, GQD might be perturbed by placing the amine group close to an oxygen rich environment (ORE).

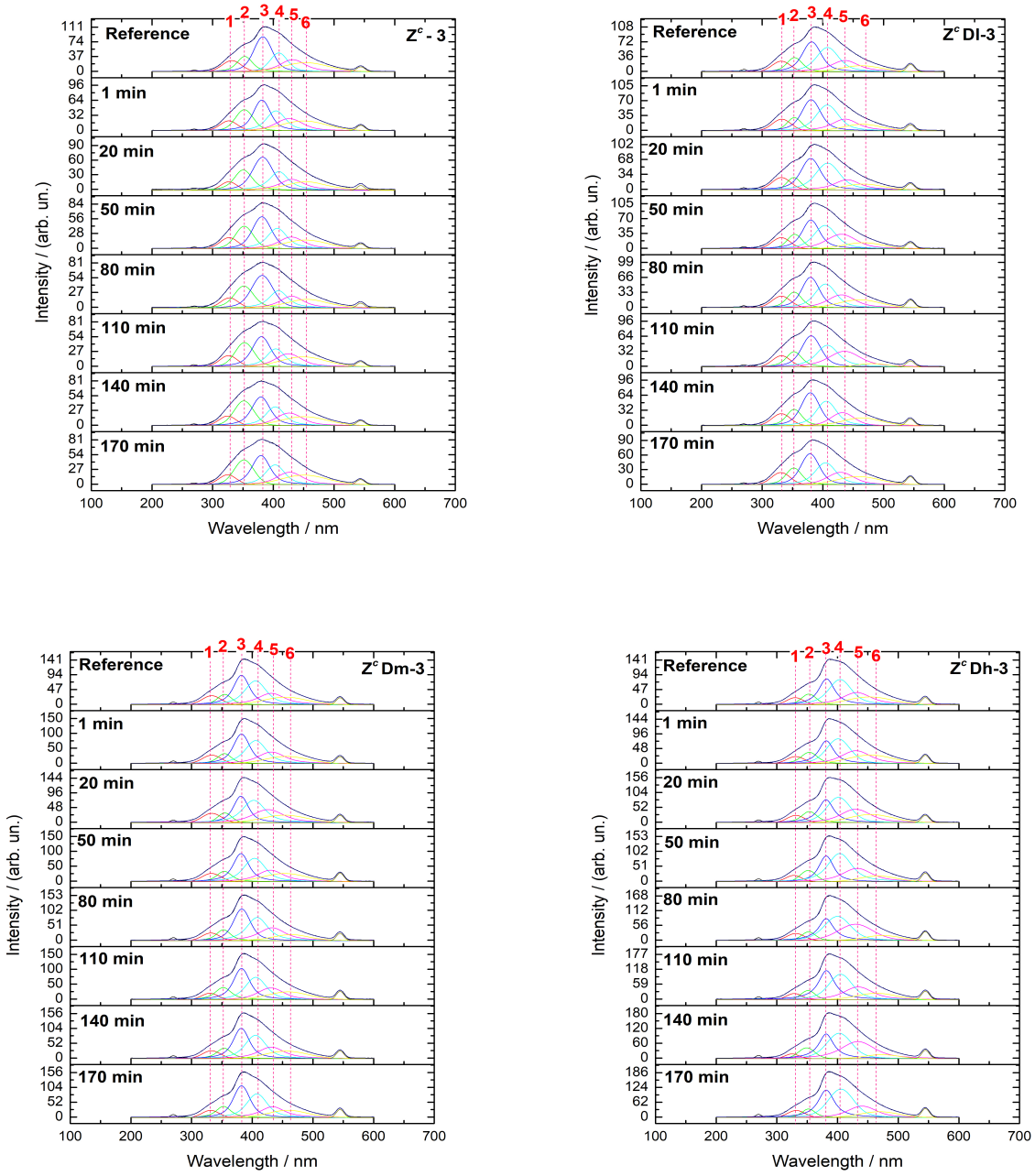

Fig. S2 PL spectra from samples Z^c-3, Z^cDl-3, Z^cDm-3 and Z^cDh-3 with respect to time evaluated at λ_{ex} = 275 nm. The first measurement was achieved as reference by only measuring the PL emission from samples prepared as in section **??**. After 1 minute, 1 mL of H_2O_2 was added to later measure spectra at every time showed in these plots. Each peak was identified with a red number at the top of each figure, corresponding to description in section **??** from manuscript

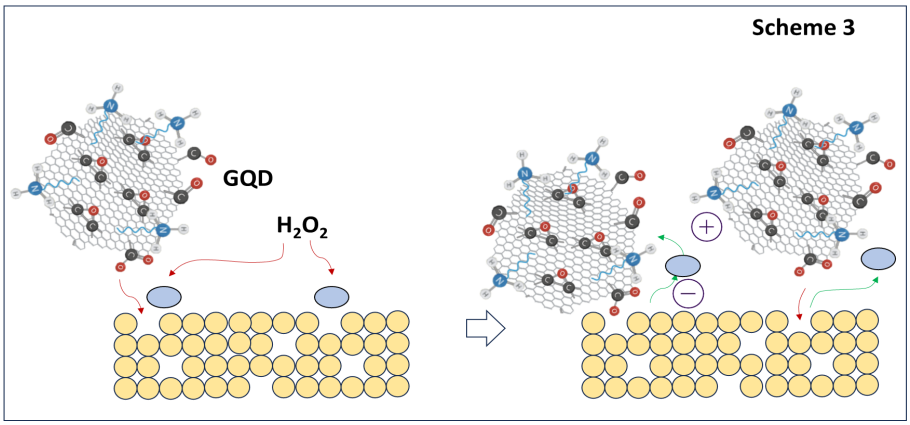

Fig. S3 This scheme 3 represents how first H_2O_2 is arriving at the ZnO surface attracted by vacancies, while not anchoring GQD later displace H_2O_2 and this oxidant might be surrounding the amine groups from GQD; other GQD might be attract by H_2O_2 which increases the amount of GQD at the ZnO surface ultimately increasing the PL emission intensity.

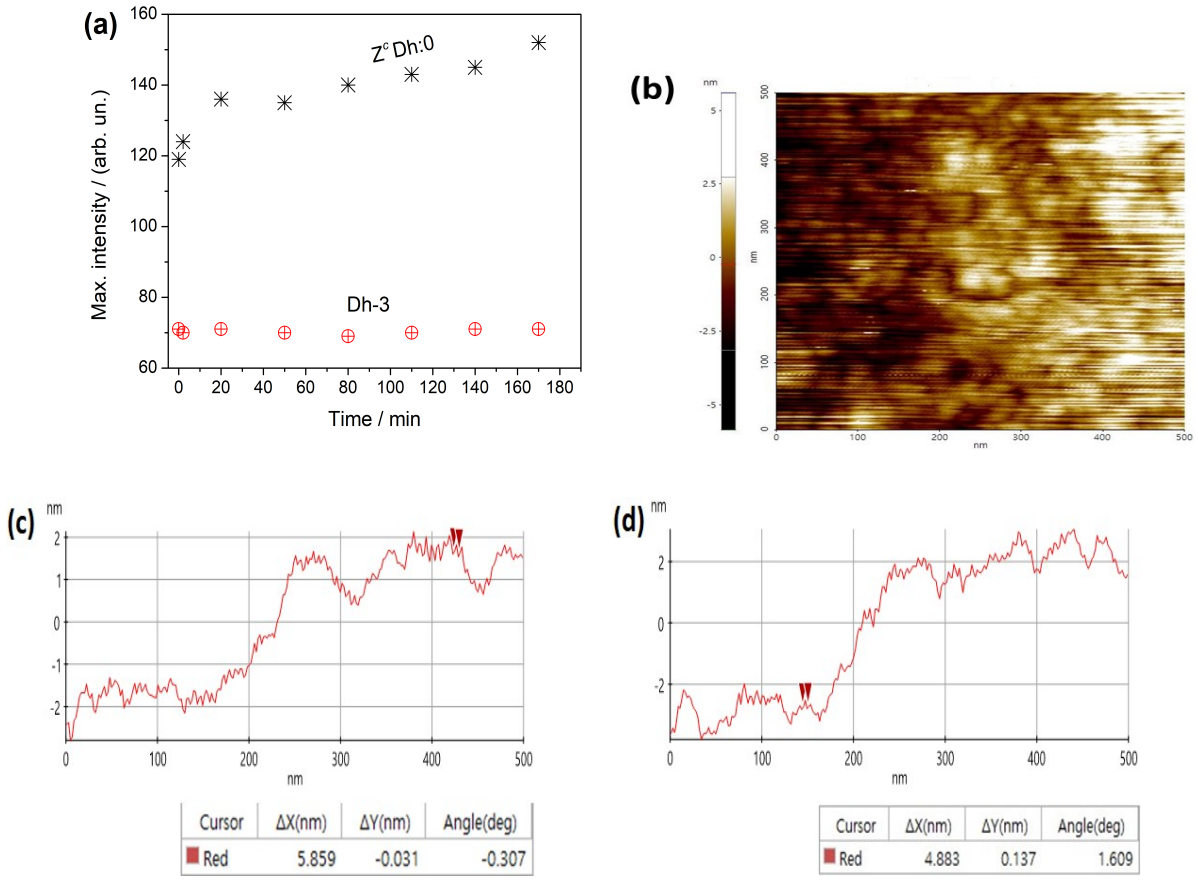

Fig. S4 (a) PL spectra for Z^{c}Dh:0 and Dh-3 taken at λ_{ex} 275 nm (b) AFM from a concentrated solution of GQD (c) and (d) GQD size estimation by the AFM software from the image displayed in (b) where graphs profiles are delimited by red cursors which represent sizes between 4 and 6 nm

The formation of *hydrozincite* may have resulted due to the presence of carbon species as contaminants supplied by the precursor zinc acetate along with hydroxyls provided principally by NaOH during the synthesis. Despite of the *hydrozincite* emergence, it is noteworthy to observe, that the ZnO phase remain as the principal structure after the drying (see Fig. **??** in manuscript).

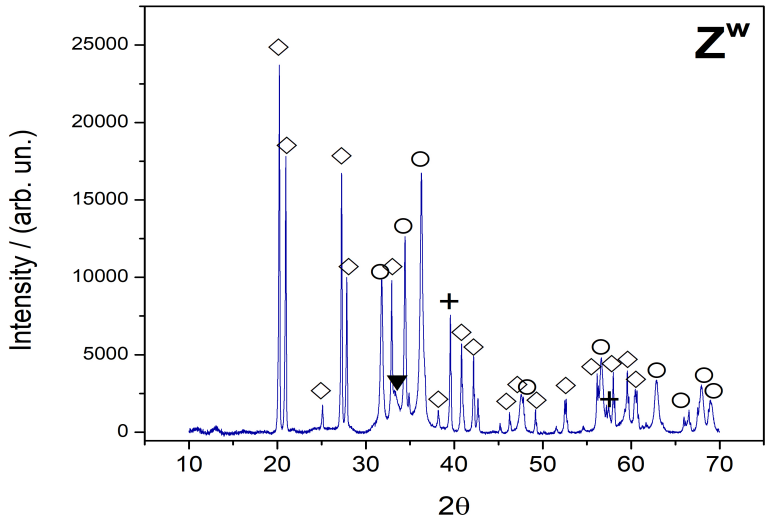

Fig. S5 XRD from Z^w; the identified phases in correspond to $Zn(OH)_2$ (⋄), ZnO or *zincite* (○), *hydrozincite* (▼) and *titanium-vanadium-aluminium* (TiVAl) (+) planes. All phases were identified by PROFEX 5.0.2 software.

To evaluate the influence of vacancies in the crystal size (D) of ZnO, higher peaks from Z^d(s), Z^c(s), Z^dDl-3(s), Z^cDl-3(s) and Z^d:1(s) (see Fig. **??** in manuscript) were taken as reference by using the Debye-Scherrer equation:

$$D = \frac{K\lambda}{\beta\, cos\theta} \tag{1}$$

where K is the Scherrer constant, λ is the wavelength of X rays source ($\lambda = 1.5405$ Å), β is the full width at half maximum and θ is the reference peak angle; results are presented in Table S1.

Table S1 Crystal size estimation obtained with ec(1). Data taken from figure **??** from manuscript

	Data		
Sample	Angle/ rad	β (FWHM[a] 10^3) / rad	Size / nm
Z^d(s)	0.3198	6.174	24.7
Z^c(s)	0.3131	7.165	21.2
Z^dDl-3(s)	0.3174	4.949	30.8
Z^cDl-3(s)	0.3114	5.640	27.0
Z^d:1(s)	0.3236	25.66	6.0

[a] FWHM: full width at half maximum

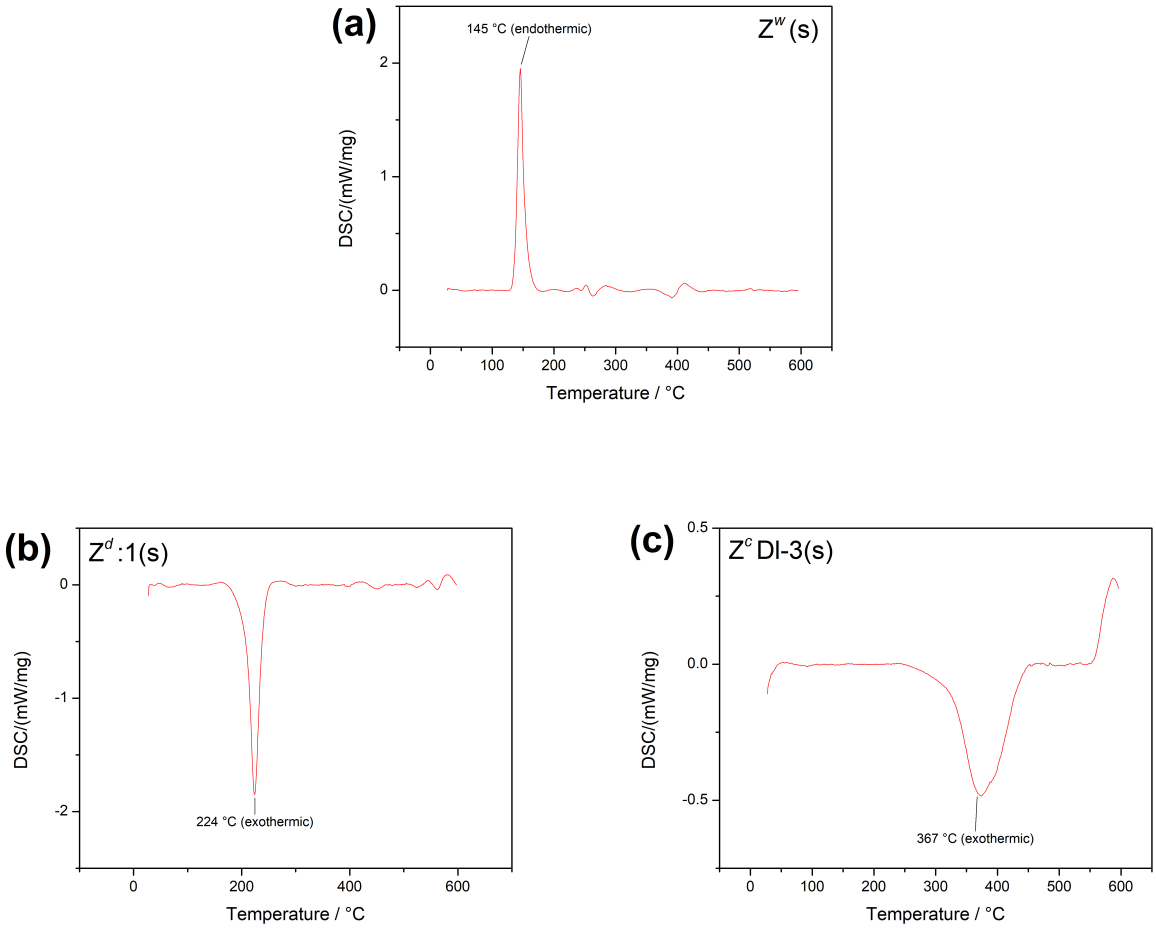

Fig. S6 Differential scanning calorimetry (DSC) for samples (a) Z^w(s) (b) Z^d:1(s) and (c) Z^cDI-3(s). For all samples the DSC test parameters were: heat rate 10 °C/min from 25 to 600 °C in a Helium atmosphere

In Fig. S6a DSC of Z^w(s) sample shows an endothermic peak at 145 °C which has been ascribed to decomposition of hydroxyl from $Zn(OH)_2$ species resulting in ZnO formation[1]. Fig. S6b shows an exothermic peak which has been related with the ZnO_2 decomposition into ZnO and oxygen[2,3]. Fig. S6c shows an exothermic peak which is assigned to decomposition of carbon and nitrogenous species chemically bonded to ZnO[4–6].

The prism and oval shapes of ZnO particles are agglomerated producing clusters with sizes of approximately 1 μm. Fig. S7a exhibits a particle from sample Z^c(l) with a diameter subtly higher than 1 μm; this particle shows extended and continuous zones where the EDS data were extracted and they are presented in the Table S2. In the elemental composition of Z^c(l), zinc and oxygen predominate, whilst the iron presence is due to contamination during the synthesis. In other zone from Z^c(l) (shown in Fig. S7b) the EDS analysis shows zinc, oxygen, carbon and silicon. Carbon and silicon are considered contaminants. Because the dissimilar amounts between zinc and carbon and the similar amounts of carbon and oxygen these contaminants can be carbonates, although contained into the liquid phase and not into the ZnO structure (Table S2). This is more evident due to in other zone from Z^c(l) (Fig. S7c) elements as magnesium and calcium were encountered; these may then be derived from magnesium and calcium carbonates salts diluted in water.

Table S2 EDS elemental analysis from SEM images in the figure S7

Sample	Figure identification	Detected elements/ w %										
		Zn	O	C	Na	Mg	Si	S	Cl	K	Ca	Fe
Z^c(l)	S7a	20.18	36.49	-	-	-	10.52	-	-	3.18	-	29.18
	S7b	9.64	36.13	49.45	-	-	4.78	-	-	-	-	-
	S7c	-	50.22	-	6.84	1.51	5.33	3.75	11.16	5.83	15.36	-
Z^c-3	S7d	27.99	32.61	39.4	-	-	-	-	-	-	-	-
	S7e	19.52	30.86	-	-	1.2	10.31	-	13.63	16.24	-	8.25
Z^cDh:0	S7f	4.94	63.4	-	-	-	19.34	-	-	6.52	5.81	-
Z^cDm-3	S7g	80.59	18.19	-	-	-	-	-	1.22	-	-	-
	S7h	76.34	19.25	-	-	-	-	-	3.34	-	1.07	-

– : not detected

EDS analysis for Z^c-3 from Fig. S7d, shows zinc, oxygen and carbon (Table S2). Again, carbon is a contaminant and it was confirmed as the chemical map in Fig. S8(2) exhibits this element at the middle of image, while oxygen and zinc are distributed over all the corresponding square (Fig. S8(3) and Fig. S8(5), respectively) however slightly concentrated where white particles lower than 1 μm from Fig. S8(1), are observed. If carbon were initially in Z^c(l), might impact on the PL properties; however, PL tests from the manuscript section **??**, demonstrate that emission originates principally from ZnO and its chemical structure environment. With the aim to finalize proving that in Z^c-3, carbon is a water contaminant during samples preparation for SEM, in Fig. S9 other type of morphology it is perceived and oxygen as zinc are uniformly spread in all the sampling zone (Fig. S9(2) and Fig. S9(9), respectively). The absence of carbon proves the PL emission is because zinc is in greater amounts. The rest of elements detected in the EDS analysis (sodium, magnesium, chloride, etc.) are also contaminants of sample (Table S2, Fig. S9).

From Fig. S7f an EDS analysis of Z^cDh:0 registered a low amount of zinc (Table S2); although this can be attributed to silicon contamination, it is highly probable that zinc is well distributed and as mentioned, in very small particles sizes distant from solid surface, making its detection difficult. Nonetheless, in the chemical map from Fig. S10 the zinc is completely dispersed in all the monitored zone.

As mentioned in the manuscript, in Z^cDm-3 the trend is the diminishing of clusters and its rupture character is also observed in Fig. S7g and Fig. S7h, which are the zones where EDS analysis were achieved. Although in these EDS carbon was not detected (Table S2) by the PL tests was evidenced its interaction in Z^cDm-3. Moreover, carbon and nitrogen from GQD was detected in XPS measurements (see section **??** in the manuscript and Fig. S14).

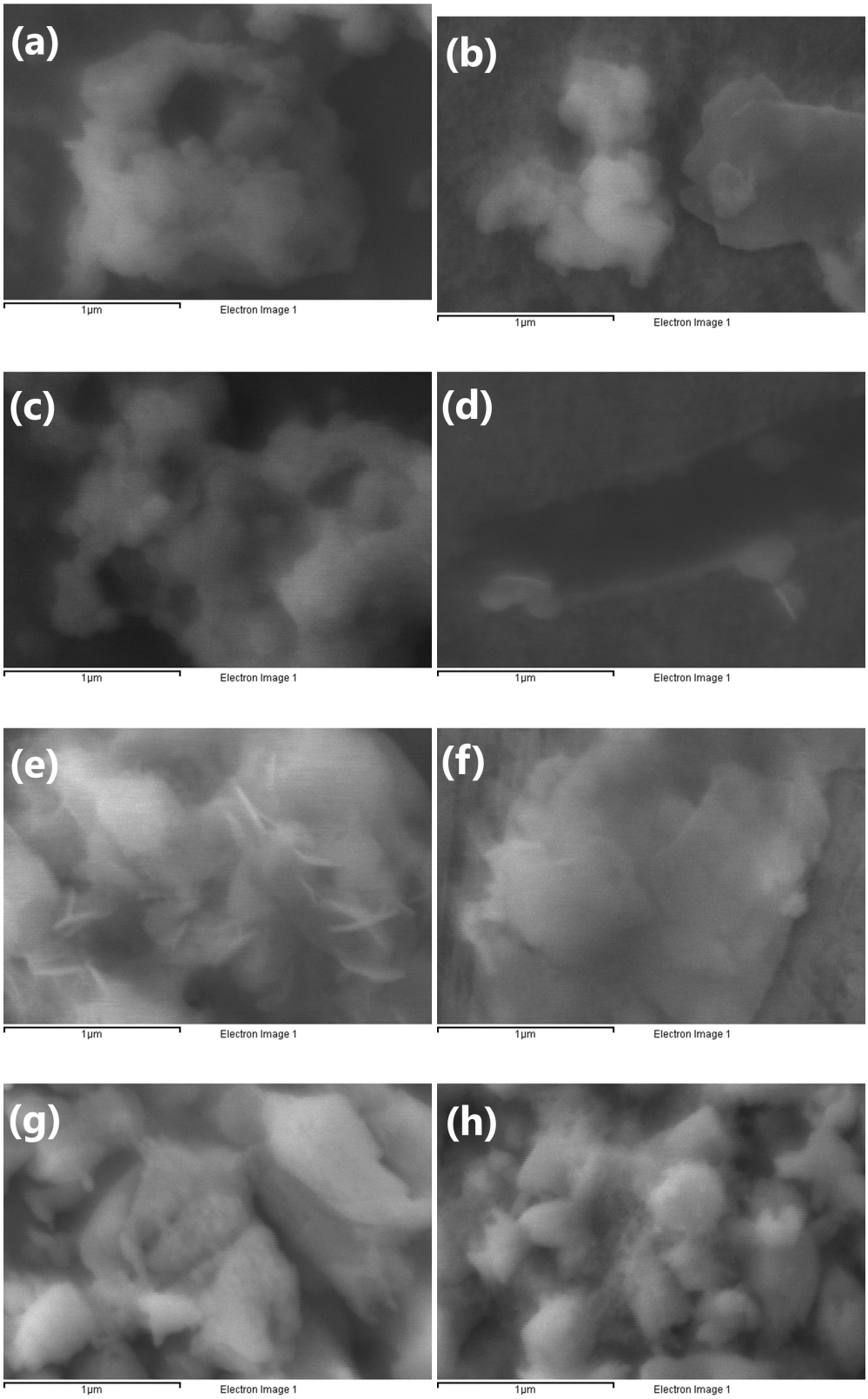

Fig. S7 FE-SEM images where EDS analysis were taken. The images correspond to Z^c(l) (a-c), Z^c-3 (d and e) Z^cDh:0 (f) and Z^cDm-3 (g and h)

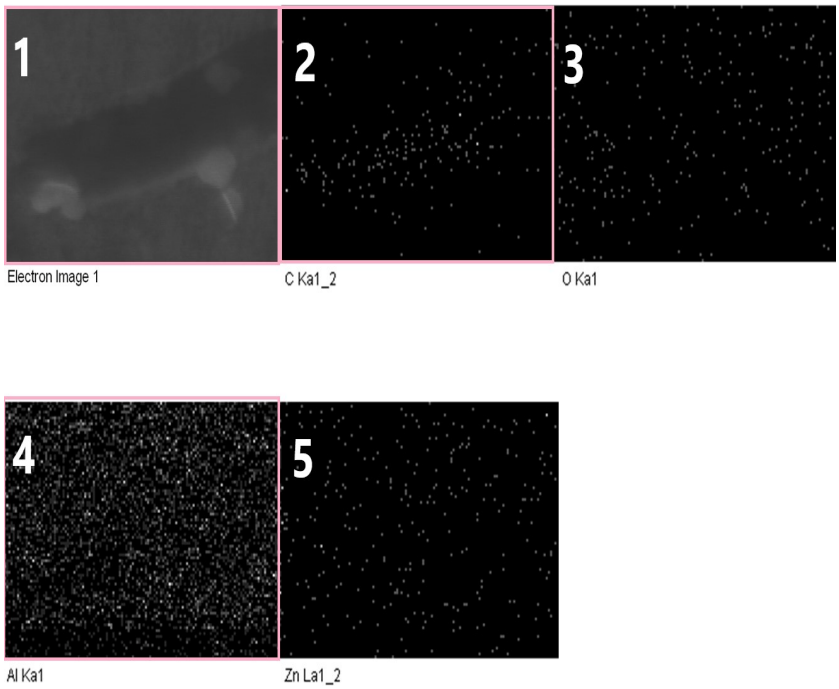

Fig. S8 Chemical elemental mapping by EDS from sample Z^c-3 which is displayed in image (1). The following images present the chemical distribution of (2) carbon, (3) oxygen, (4) aluminium (substrate), (5) zinc, detected on the sampling area

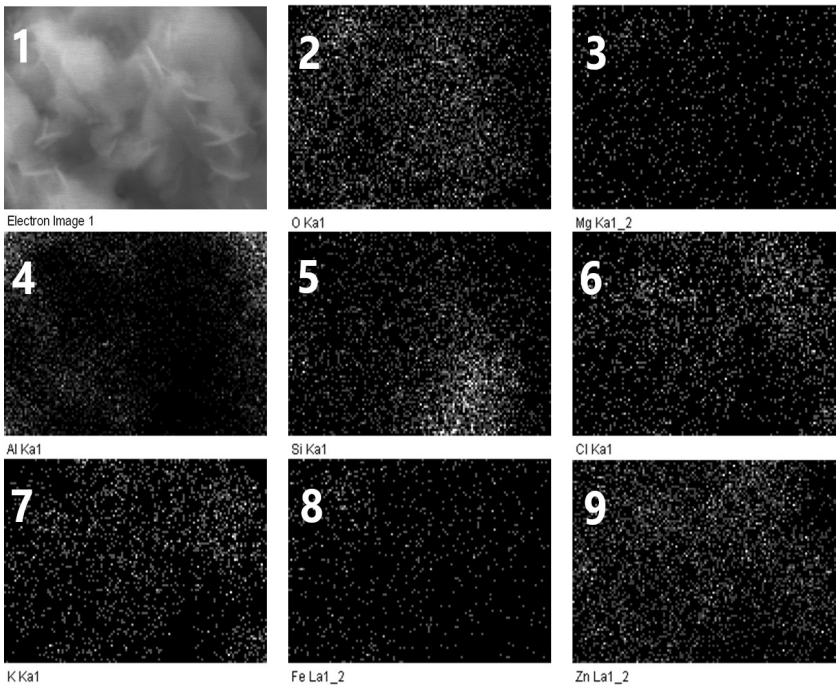

Fig. S9 Chemical elemental mapping by EDS from sample Z^c-3 which is displayed in image (1). The following images present the chemical distribution of (2) oxygen, (3) magnesium, (4) aluminium (substrate), (5) silicon, (6) chloride, (7) potassium (8) iron and (9) zinc, detected on the sampling area

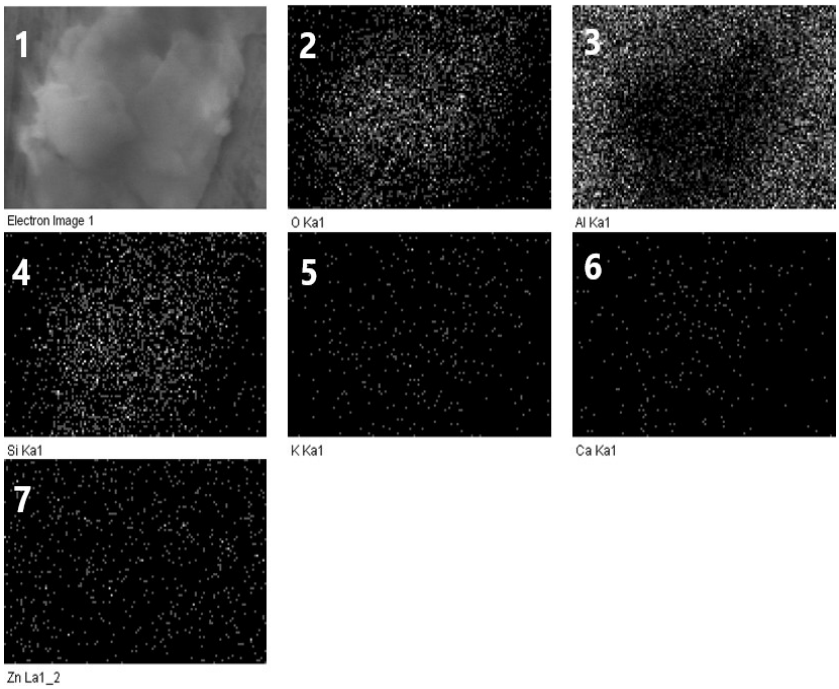

Fig. S10 Chemical elemental mapping by EDS from sample Z^cDh:0 which is displayed in image (1). The following images present the chemical distribution of (2) oxygen, (3) aluminium (substrate), (4) silicon, (5) potassium (6) calcium and (7) zinc, detected on the sampling area

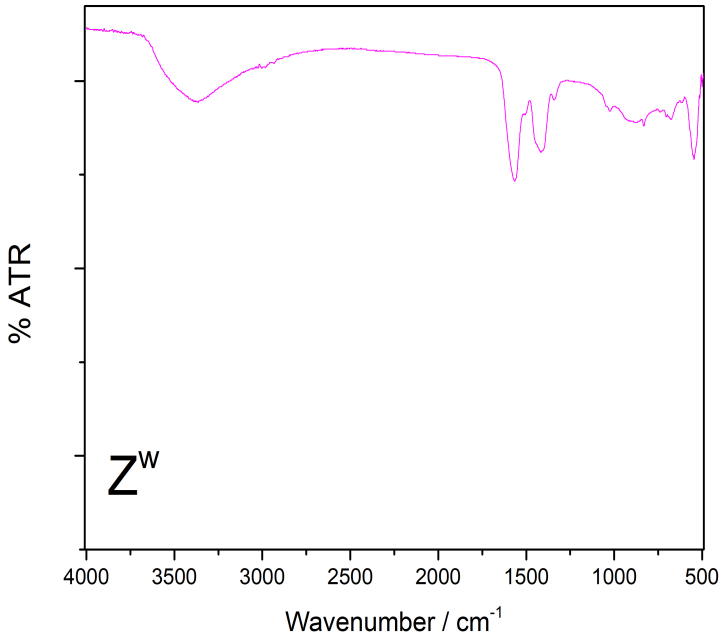

Fig. S11 FTIR spectrum, both for Z^{w} which superscript "w" represents wet conditions for zinc nanoparticles as synthesized without any further heat treatment.

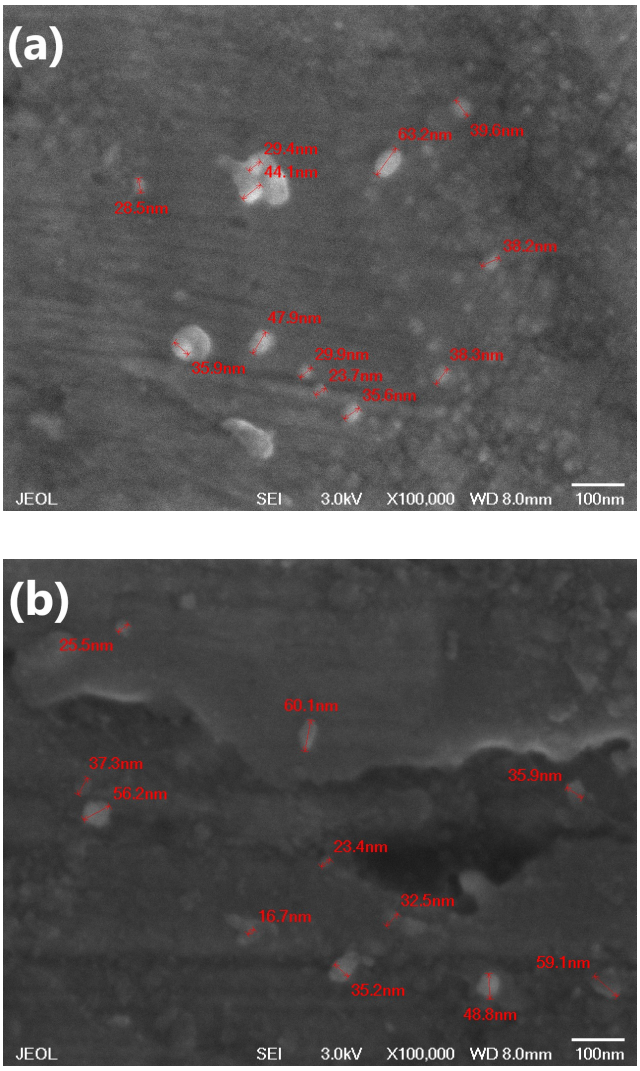

Fig. S12 SEM images from (a) Dl and (b) Dh. Both were taken directly from their corresponding solutions without H_2O_2 exposure

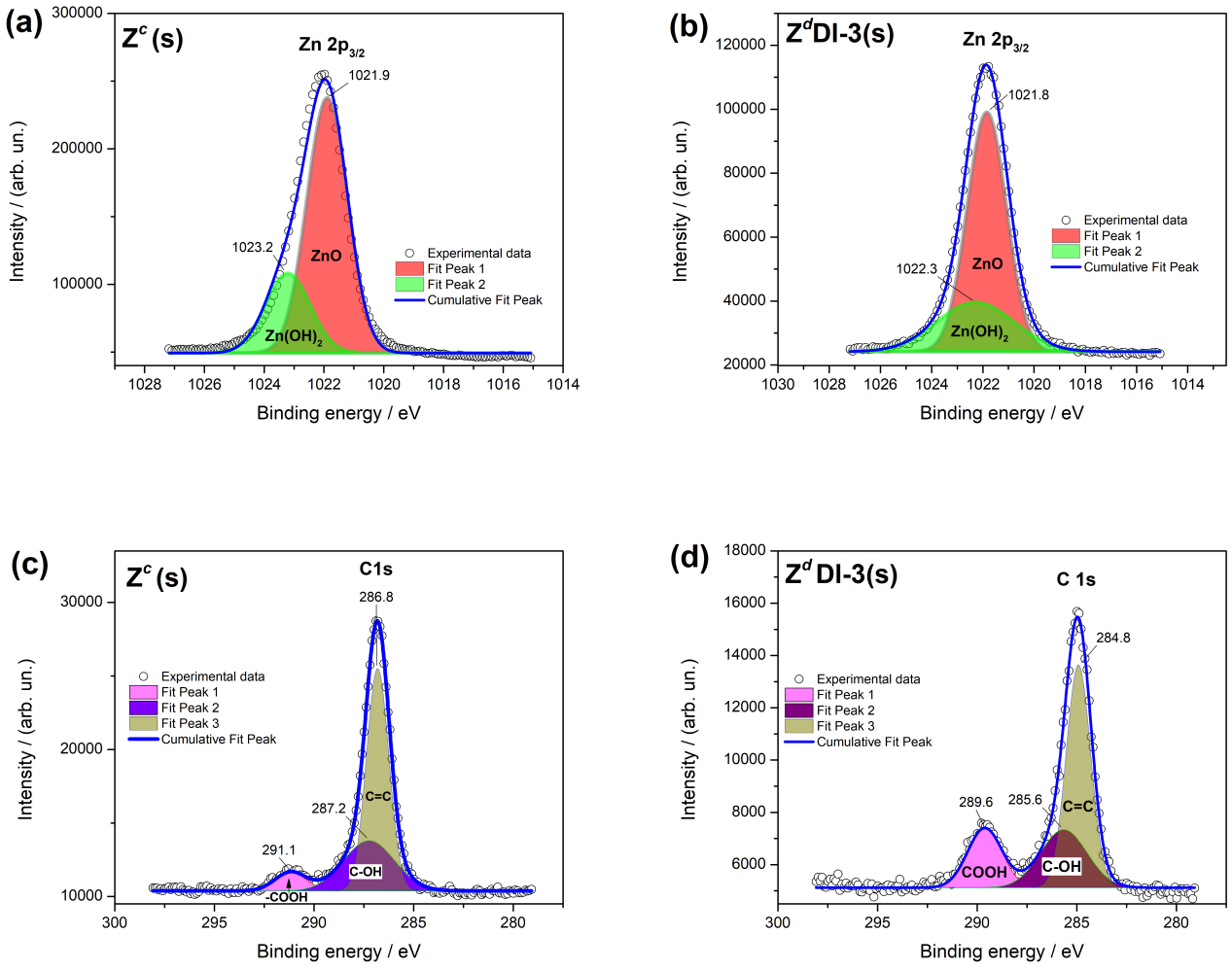

Fig. S13 XPS spectra of zinc peak ($Zn2p_{3/2}$) in (a) Z^c(s) and (b) Z^dDI-3(s), and for carbon peak (C1s) in (c) Z^c(s) and (d) Z^dDI-3(s)

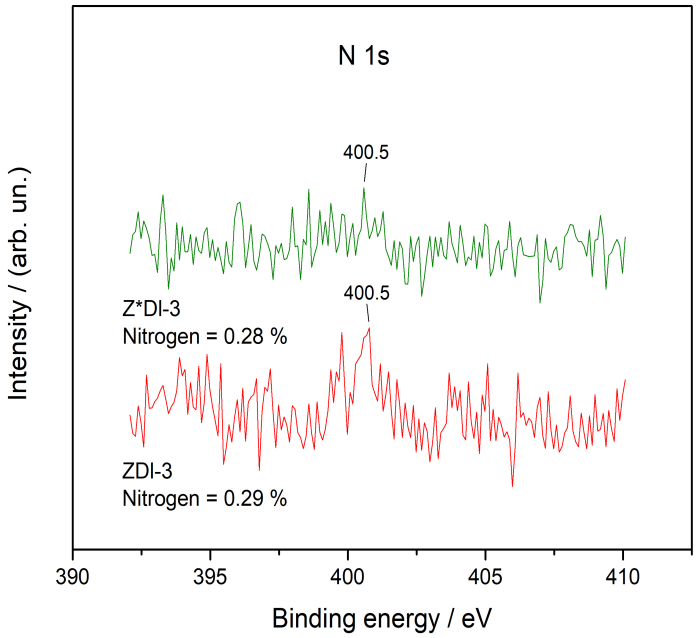

Fig. S14 XPS spectra for samples Z^{c}DI-3(s) and Z^{d}DI-3(s) showing the nitrogen peak (N1s) detected by the equipment.

Notes and references

1 A. Gordeeva, Y.-J. Hsu, I. Z. Jenei, P. H. B. Brant Carvalho, S. I. Simak, O. Andersson, U. Häussermann, Layered Zinc Hydroxide Dihydrate, $Zn_5(OH)_{10}{\cdot}2H_2O$, from Hydrothermal Conversion of ε-$Zn(OH)_2$ at Gigapascal Pressures and its Transformation to Nanocrystalline ZnO, ACS Omega 5 (28) (2020) 17617–17627. doi:10.1021/acsomega.0c02075.

2 S. Ali, R. Morsy, N. El-Zawawy, M. Fareed, M. Bedaiwy, Synthesized zinc peroxide nanoparticles (ZnO_2;-NPs): a novel antimicrobial, anti-elastase, anti-keratinase, and anti-inflammatory approach toward polymicrobial burn wounds, International Journal of Nanomedicine Volume 12 (2017) 6059–6073. doi:10.2147/ijn.s141201.

3 V. Alvarado-Pérez, L. I. Cabrera-Lara, G. López-Téllez, D. Mendoza-Anaya, S. Hernández-López, M. Camacho-López, ZnO to ZnO_2 transformation assisted by H_2O_2 at ambient conditions, Materials Chemistry and Physics 233 (2019) 180–184. doi:10.1016/j.matchemphys.2019.05.066.

4 A. Tayyebi, M. outokesh, M. Tayebi, A. Shafikhani, S. S. Şengör, ZnO quantum dots-graphene composites: Formation mechanism and enhanced photocatalytic activity for degradation of methyl orange dye, Journal of Alloys and Compounds 663 (2016) 738–749. doi:10.1016/j.jallcom.2015.12.169.

5 M. Pudukudy, Z. Yaakob, R. Rajendran, T. Kandaramath, Photodegradation of methylene blue over novel 3D ZnO microflowers with hexagonal pyramid-like petals, Reaction Kinetics, Mechanisms and Catalysis 112 (2) (2014) 527–542. doi:10.1007/s11144-014-0703-5.

6 K. E. Levine, B. J. Collins, M. D. Stout, M. Wyde, S. E. Afton, A. S. Essader, T. J. Ennis, K. E. Amato, A. C. McWilliams, B. L. Fletcher, R. A. Fernando, J. M. Harrington, N. Catlin, V. G. Robinson, S. Waidyanatha, Characterization of zinc carbonate basic as a source of zinc in a rodent study investigating the effects of dietary deficiency or excess, Analytical Letters 50 (15) (2017) 2447–2464. doi:10.1080/00032719.2017.1293073.